Journal of
Materials Chemistry A

ROYAL SOCIETY
OF CHEMISTRY

PAPER

View Article Online
View Journal | View Issue

Check for updates

Cite this: *J. Mater. Chem. A*, 2025, **13**, 41019

Multiple-crosslinking-reinforced ionogel electrolytes for safe and high-performance quasi-solid-state lithium metal batteries

Jiaqi Huang,[a] Yin Hu,[ab] Qingwei Gao,[c] Yupo She,[b] Jiajia Li,[a] Haiman Hu,[a] Huaiyang Zheng,[a] Feng Yan *[b] and Xiaoyan Ji *[a]

Received 17th September 2025
Accepted 23rd October 2025

DOI: 10.1039/d5ta07159c

rsc.li/materials-a

Quasi-solid polymer electrolytes (QSPEs) are promising electrolytes for next-generation high-energy-density lithium metal batteries, benefiting from their flexibility and intimate interfacial contact with electrodes. However, conventional QSPEs encounter challenges such as limited Li^+ mobility and poor mechanical properties. Herein, we design a multiple-crosslinked ionogel electrolyte, featuring a high Li^+ transference number of 0.74, superior stability against oxidation up to 4.8 V, and high mechanical strength (0.8 MPa) simultaneously. The ionogel electrolyte constructs rapid Li^+ conductive pathways and promotes the formation of lithium fluoride (LiF), lithium nitride (Li_3N), and lithium sulfide (Li_2S)-enriched passivation layers during Li deposition, greatly enhancing the reversibility of lithium metal deposition. Consequently, the Li||Li cell demonstrates superior lithium plating/stripping stability for 5000 h, and the Li||$LiFePO_4$ cell shows stable cycling performance with 80% capacity retention after 1000 cycles at a rate of 0.5C. Remarkably, the high-voltage Li||NCM532 cell maintains about 76% of its capacity over 200 cycles at 4.2 V.

Introduction

Lithium-based rechargeable batteries are emerging as promising energy storage devices, offering advantages over traditional systems owing to their lightweight, minimal maintenance, superior energy density, and high electrochemical potential.[1,2] As the "holy grail" of anodes, lithium metal electrodes receive much attention on account of their exceptional theoretical specific capacity (3860 mAh g^{-1}) and relatively low redox potential (−3.040 V).[3,4] Nevertheless, the utilization of liquid electrolytes (LEs) in lithium metal batteries (LMBs) increases the risk of safety incidents, such as fires and explosions, limiting the battery's long-term cycling performance.[5,6] Furthermore, LEs can barely withstand elevated operating voltage and undergo reactions with Li anodes, resulting in fragile solid electrolyte interphase (SEI) layers and uncontrolled deleterious lithium dendrites.[7,8]

By eliminating flammable organic solvents, polymer solid electrolytes (PSEs) offer a reliable solution to address critical concerns, including the suppression of transition metal cation dissolution and parasitic reactions on the surface of the electrodes.[9–11] However, due to the high crystallization, their commercial viability is hindered by limited ionic conductivity (10^{-6}–10^{-7} S cm^{-1}) at ambient temperature.[12,13] To overcome this challenge, many strategies have been developed to reduce the polymer crystallization or enrich the ionic transfer pathways, such as designing polymer structures, incorporating LEs, using cross-linking, and introducing fillers.[14–17] Among these, gel polymer electrolytes (GPEs), composed of polymer frameworks and supporting electrolytes, have emerged as a viable alternative, exhibiting high ionic conductivity.[18,19] Commonly, organogel electrolytes integrate polymer frameworks with organic molecules to form microporous channels for ions to migrate freely between the electrodes. For instance, *in situ* polymerization of the methyl methacrylate monomer in a liquid dimethoxyethane (DME)-based GPE has been utilized to regulate lithium-ion (Li^+) transport. The resulting quasi-solid GPE traps PF_6^- anions and free DME molecules *via* hydrogen bonds, leading to improved ionic conductivity (7.49×10^{-3} S cm^{-1}) and an enhanced Li^+ transference number (t_{Li^+}) of 0.48.[20] Similarly, GPEs incorporating ether-based liquids into stable cross-linked amide frameworks exhibit high ionic conductivity (1.76×10^{-3} S cm^{-1}) and an increased Li^+ transference number (t_{Li^+}) of 0.78.[21] However, conventional GPEs typically rely on organic solvents, and these solvents are often flammable, posing safety hazards, and can trigger interfacial instability and side reactions with lithium metal, leading to dendrite growth, electrolyte decomposition, and capacity fading.

---

[a] *Energy Engineering, Division of Energy Science, Luleå University of Technology, Luleå 97187, Sweden. E-mail: xiaoyan.ji@ltu.se*

[b] *College of Chemistry, Chemical Engineering and Materials Science, Soochow University, Suzhou, 215123, China. E-mail: fyan@suda.edu.cn*

[c] *Shanghai Key Laboratory of Materials Protection and Advanced Materials in Electric Power, Shanghai University of Electric Power, Shanghai 201306, China*

In this regard, ionogel electrolytes (IGEs) incorporating ionic liquids (ILs) offer several advantages, including excellent electrochemical stability, non-flammability, high polarity to dissociated lithium salts, and fewer side reactions,[22,23] which can offset their higher material costs. IGEs have been engineered with tailored polymer networks that integrate complementary properties, such as combining mechanical flexibility with structural rigidity and preserving continuous pathways for efficient Li^+ transport.[24–26] However, precisely regulating the ion environment to achieve high Li^+ conductivity, robust mechanical strength, and superior oxidative stability remains a key challenge for the development of safe and high-energy-density batteries.

Herein, a multiple-crosslinked ionogel was prepared *via* the copolymerization of 1-vinyl-3-ethoxy-methyl-imidazolium bis(trifluoromethylsulfonyl)imide (VOMImTFSI), pentaerythritol tetraacrylate (PET4A), and polyethylene glycol diacrylate (PEGDA), along with lithium bis(fluorosulfonyl)imide (LiFSI) and *N*-butyl-*N*-methylpyrrolidinium bis(fluorosulfonyl)imide ($Pyr_{13}FSI$) as supporting electrolytes. The copolymerization engages the covalent cross-linking chain with a four-arm PET4A and intermolecular hydrogen bonding between imidazolium cations and ether units, constructing robust polymer frameworks to provide superior mechanical stability. The metal ion–anion–polycation coordination structure constructs rapid Li^+ transport channels and supports the establishment of a robust inorganic-enriched SEI. The ionogel electrolytes display stable, low overpotential, and long-term reversible Li plating/stripping for 5000 h in Li||Li symmetrical cells. The Li||$LiFePO_4$ (LFP) cell can be stably cycled for 1000 cycles with a capacity retention of about 80%. Additionally, the 4.2 V Li||$LiNi_{0.5}Co_{0.2}Mn_{0.3}O_2$ (NCM532) cells deliver a superior capacity retention of about 76% after 200 cycles. The polymerization and film-casting processes are compatible with conventional battery manufacturing, using commercially available materials under mild conditions without expensive catalysts. These features indicate that the ionogel electrolyte is cost-effective and scalable, supporting its industrial relevance for high-performance quasi-solid-state lithium metal batteries.

Results and discussion

Ionogel electrolyte synthesis and electrochemical properties

Fig. 1a illustrates a diagram outlining the fabrication process of ionogel electrolytes. VOMImTFSI was copolymerized with the supramolecular cross-linker PET4A and PEGDA, incorporating 20 wt% $Pyr_{13}FSI$ (^1H nuclear magnetic resonance spectroscopy (NMR) is illustrated in Fig. S1), as supporting electrolytes, to obtain a mechanically strong ionogel electrolyte. Fourier transform infrared spectroscopy (FT-IR) (Fig. S2a) was applied to analyze the chemical structure of every single composition in the electrolyte system. The magnified FT-IR spectra in Fig. S2b show that the vinyl-related C=C peak from VOMImTFSI, PET4A, and PEGDA at 1655 cm^{-1} disappears,[27] confirming the occurrence of chemical cross-linking through the polymerization of the vinyl groups. Moreover, as shown in Fig. S3, the addition of PEGDA causes a downfield chemical shift in ^1H NMR, indicating the formation of a hydrogen bonding interaction between the oxygen atoms in the alkoxy chains and the imidazolium C–H groups.[28,29] Together with the ion–ion coordination between polycations, anions, and Li^+, these physical cross-links complement the chemical network, contributing to the formation of multiple-crosslinked ionogel electrolytes, simultaneously boosting mechanical robustness and Li^+ transport.

The prepared ionogel electrolyte, denoted as IGE-2, was characterized to evaluate its properties and performance, and ionogel electrolytes with different $Pyr_{13}FSI$ contents (0 wt% denoted as PE and 10 wt% denoted as IGE-1) were prepared for comparison. The thermal stability of the different electrolytes was measured *via* thermogravimetric analysis (TGA). The thermograms of the electrolytes under N_2 and air atmospheres are presented in Fig. S4 and S5, respectively. The thermal degradation temperature of IGE-2 exceeds 267 °C in both N_2 and air atmospheres, and all other electrolytes reveal excellent thermal stability with similar decomposition temperatures to IGE-2, indicating a high pyrolysis temperature of the electrolytes. These results confirm the thermal stability of the ionogel electrolytes, reinforcing their suitability for battery applications at elevated temperatures. Additionally, IGE-2 exhibited non-flammability and did not ignite upon exposure to an open flame (Fig. S6). The non-flammability is attributed to the inherent stability of both the polymer backbone and $Pyr_{13}FSI$, underscoring its safety advantages for practical applications. Furthermore, differential scanning calorimetry (DSC) analysis was conducted to evaluate the melting temperature (T_m) and glass transition temperature (T_g) of the electrolytes under a N_2 flow. As depicted in Fig. S7, PE exhibits a distinct T_m of 222.8 °C, which is advantageous for maintaining structural stability. The incorporation of IL maintains this structural stability. Additionally, the T_g of PE is approximately −10.6 °C, while those of IGE-1 and IGE-2 are −24.2 and −27.3 °C, respectively. Additionally, as depicted in Fig. S8, the DSC of IGE-2 was tested under an air atmosphere, which shows a T_g of −27.6 °C, similar to the results obtained under a N_2 flow. The introduction of $Pyr_{13}FSI$ further decreases the T_g of the electrolytes, which enhances ionic mobility by promoting the segmental flexibility of polymer chains.[30] Furthermore, density functional theory (DFT) suggests that the reduction in T_g is associated with enhanced metal ion–anion–polycation co-coordination (Fig. S9a and 9b). The binding energy of the metal ion–anion–polycation complex is −348.81 kJ mol^{-1}, which is lower than that of the anion–polycation interaction (−359.91 kJ mol^{-1}). The increase in coordination weakens the anion–polycation interactions and reduces the ionic crosslinking between polymer chains, thereby facilitating local segmental dynamics and increasing ionic mobility in IGE-2.[31]

Tensile experiments were performed to quantitatively assess the mechanical properties of the prepared films. As shown in Fig. 1b, PE exhibits a high tensile modulus of 1.2 MPa, exceeding that of conventional PEO/LiTFSI-based PSEs by more than twofold,[32] but its strain elongation rate is only 35%. With the incorporation of IL, the mechanical strength of IGE-1 decreases slightly to 0.8 MPa while elongation increases to

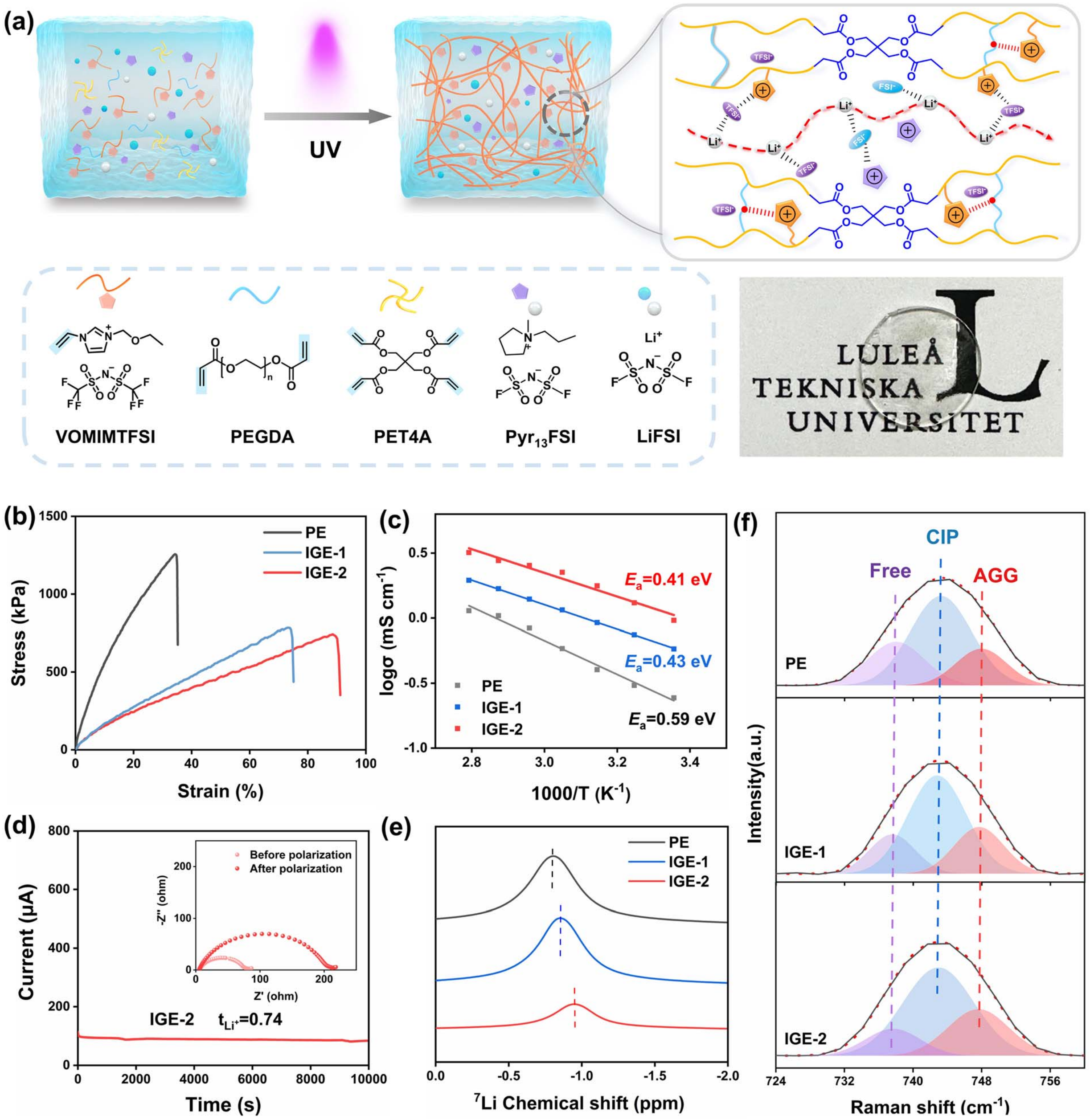

Fig. 1 (a) Schematic of synthesizing an ionogel electrolyte (inset shows the macroscopy image of the ionogel electrolyte). (b) Stress–strain plots of PE, IGE-1, and IGE-2. (c) Arrhenius curves of the variation in ionic conductivity with different temperatures for PE, IGE-1, and IGE-2. (d) The Li^+ transference number of IGE-2. (e) ^7Li solid-state NMR spectra of PE, IGE-1, and IGE-2. (f) Raman spectra of PE, IGE-1, and IGE-2.

75%. Further increasing the IL content, IGE-2 maintains the mechanical strength of IGE-1 while further enhancing the strain elongation rate to 90%. The presence of the IL monomer contributes to the improved elongation at break. However, when the IL content is further increased to 30 wt% (IGE-3), both mechanical strength and strain begin to decline due to potential over-softening of the electrolyte (Fig. S10). The synergistic balance between the chemical cross-linking, driven by the four-arm structure of PET4A and VOMImTFSI, and the physical cross-linking, arising from hydrogen bonding, endows IGE-2 with mechanical robustness.[33,34] The ionogel achieves a balanced combination of mechanical resilience and Li^+ transport through multi-level interactions. The synergistic balance between the chemical cross-linking, driven by the four-arm structure of PET4A and VOMImTFSI, and the physical cross-linking, arising from hydrogen bonding and metal ion–anion–polycation co-coordination, endows IGE-2 with mechanical robustness.

Fig. 1c shows the ionic conductivity of the prepared electrolyte. PE demonstrates an ionic conductivity of 2.44×10^{-4} S cm^{-1} at 25 °C. By incorporating the IL into PE, the ionic conductivity of IGE-1 and IGE-2 increases significantly to 5.82 ×

10^{-4} and 9.58×10^{-4} S cm^{-1} at 25 °C, respectively. The improved ionic conductivity of IGE-2 is due to the low T_g and poly VOMIm$^+$–anion–Li$^+$ co-coordination. The activation energy (E_a) values, determined by fitting the ionic conductivity data with the VTF equation, are 0.59 eV for PE, 0.43 eV for IGE-1, and 0.41 eV for IGE-2, indicating a reduced energy barrier for Li$^+$ transport with IL incorporation. Furthermore, the t_{Li^+} is determined using the Bruce–Vincent method.[35] As illustrated in Fig. 1d, the initial current is 112.8 μA, stabilizing at 83.3 μA after polarization, with the interfacial impedance increasing from 64.6 to 181.7 Ω. The t_{Li^+} for IGE-2 was calculated to be 0.74, significantly higher than those of IGE-1 (0.65, Fig. S11a) and PE (0.24, Fig. S11b), with detailed data provided in Table S1. Moreover, the metal ion–anion–polycation coordination lowers the T_g, enhancing polymer chain segment mobility and providing continuous pathways for rapid Li$^+$ transport.

The improved ionic conductivity and t_{Li^+} can be ascribed to the improved Li$^+$ mobility and Li$^+$ transport sites in IGE-2, as confirmed by ^{7}Li solid-state NMR and Raman spectroscopy. As shown in Fig. 1e, the ^{7}Li peak shifts upfield with increasing IL content, indicating a strengthened shielding effect on Li$^+$, corresponding to the enhanced coordination of FSI$^-$/TFSI$^-$ with Li$^+$.[36,37] The enhanced coordination lowers the lowest unoccupied molecular orbital (LUMO) of FSI$^-$/TFSI$^-$, thereby facilitating their decomposition and forming a LiF and LiNO$_3^-$ enriched SEI on the lithium metal electrode surface.[38] To further investigate the solvation environment among the polymer, IL, and Li salt, as well as its impact on ionic conductivity and t_{Li^+}, Raman spectroscopy was conducted. As shown in Fig. S12, the peaks at (742–744 cm^{-1}) can be ascribed to LiTFSI and LiFSI,[39–41] and Fig. 1f presents the solvation structures of PE, IGE-1, and IGE-2. The peaks observed at 737, 743 and 748 cm^{-1} are associated with free ion pairs, contact ion pairs (CIP) and aggregated ion pairs (AGG),[42] respectively. As the IL content increases, the overall intensity of the free FSI$^-$/TFSI$^-$ peak decreases from 34.1% (PE) to 18.7% (IGE-1) and further to 14.5% (IGE-2). This reduction reflects a substantial increase in CIP- and AGG-coordinated FSI$^-$/TFSI$^-$, promoting the formation of additional Li$^+$ transport sites in IGE-2 that enhance both ionic conductivity and t_{Li^+}.[43]

These findings are consistent with results from molecular dynamics (MD) simulations. Fig. 2a and b depict the IGE-2 and PE models, respectively. Mean-square displacement (MSD) analysis reveals that Li$^+$ exhibits higher mobility in IGE-2 compared to PE (Fig. 2c). Furthermore, as depicted in Fig. 2d, the diffusion coefficient of Li$^+$ in IGE-2 reaches 2.270×10^{-3}, which is significantly higher than that in PE (1.502×10^{-4}), indicating enhanced Li$^+$ diffusion dynamics in IGE-2. To further investigate the ion coordination environments, the radial distribution function (RDF, $g(r)$) was analyzed. Fig. 2e shows the RDFs calculated between Li$^+$ and FSI$^-$. The RDF peaks at 0.20, 0.36 and 0.44 nm are related to the different Li$^+$–FSI$^-$ coordination geometries. The more prominent RDF peaks of Li$^+$–FSI$^-$ in IGE-2 suggest that the introduction of Pyr$_{13}$FSI facilitates the incorporation of more FSI$^-$ anions into the Li$^+$ solvation shell, leading to a molten Li–FSI salt-dominated chemical environment observed in the superconcentrated IL electrolytes, which can promote the Li$^+$ diffusion.[44,45] Furthermore, the RDF analysis in Fig. 2f reveals the coordination behavior between Li$^+$ and TFSI$^-$ on the polyIL. The decreased RDF peaks of Li$^+$–TFSI$^-$ in IGE-2 compared to PE indicate a weakened binding strength between Li$^+$ and polyIL. These results suggest that the

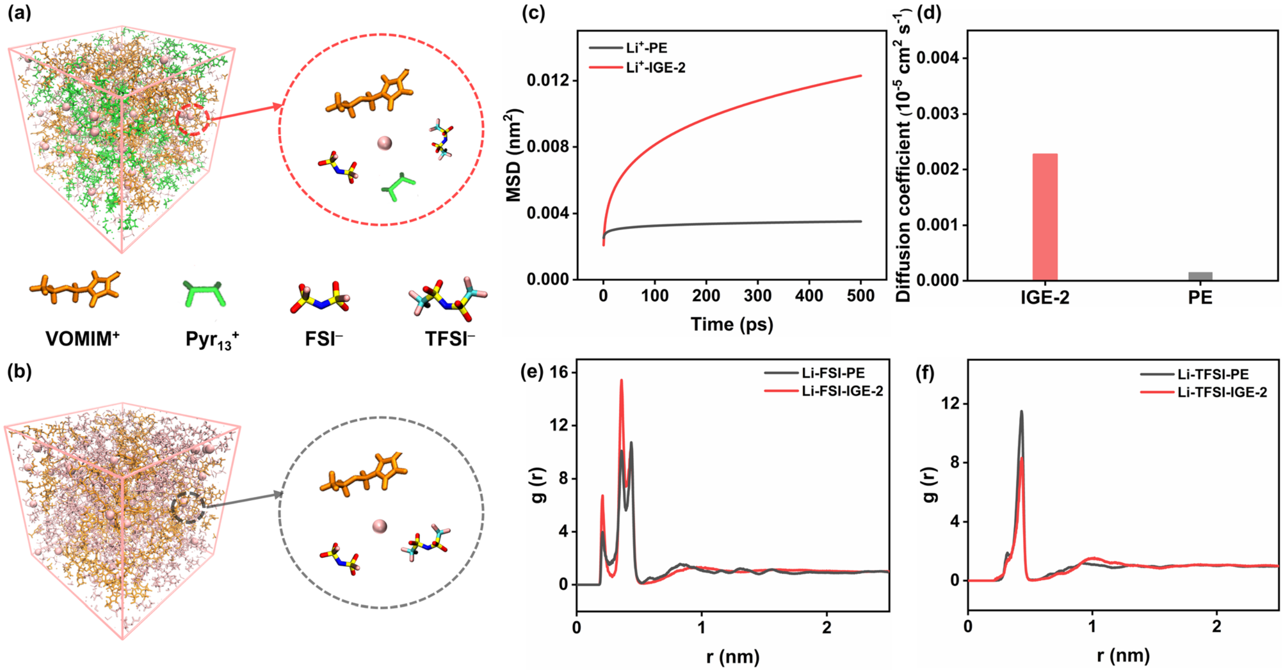

Fig. 2 MD snapshots showing the structures of (a) IGE-2 and (b) PE. (c) MSD profiles of Li$^+$ in IGE-2 and PE were obtained from MD simulations. (d) Diffusion coefficients of IGE-2 and PE. Calculated RDFs of (e) LiFSI and (f) LiTFSI with IGE-2 and PE.

formation of molten salt-like regions in IGE-2, combined with the reduced Li^+–polyIL interaction, effectively facilitates Li^+ diffusion within the ionogel matrix.

Lithium metal compatibility of the ionogel electrolyte

Fig. 3a shows the electrolyte stability with Li metal, and the Tafel plots reveal a higher exchange current density of 0.082 mA cm^{-2} for IGE-2 in contrast to 0.006 mA cm^{-2} for PE, demonstrating enhanced Li^+ transport kinetics and accelerated Li^+ migration with Li metal and IGE-2.[46] To further evaluate the compatibility between PE/IGE-2 and the Li metal, the cycling stability of symmetric Li‖Li batteries was assessed at 60 °C. Critical current density (CCD) measurements (Fig. 3b and S13) were performed to determine the optimal current density of Li‖Li plating/stripping. Employing a stepwise current increment of 0.025 mA cm^{-2} per cycle, the potential response adheres closely to Ohm's law, confirming stable operation within a current density below 0.80 mA cm^{-2} of IGE-2 and a lower range of 0.20 mA cm^{-2} for PE.[47,48] Further galvanostatic cycling tests (Fig. 3c) were performed at various currents of 0.05 to 0.15 mA cm^{-2} (areal capacities of 0.1 to 0.3 mAh cm^{-2}). The Li|PE|Li cell displays pronounced voltage fluctuations, indicative of unstable interfacial behavior. In comparison, the Li|IGE-2|Li cell maintains stable overpotentials of approximately 43 and 70 mV for capacities of 0.2 and 0.3 mAh cm^{-2}, respectively. When the capacity is reduced back to 0.1 mAh cm^{-2}, the overpotential recovers to 26 mV and remains stable for 1000 h, which is nearly twice the operational duration of the Li|PE|Li cell under the same conditions.

The long cycling stability of symmetric Li‖Li batteries was investigated with IGE-2. The cell exhibits high stability, maintaining consistent performance for 5000 h at a current density of 0.05 mA cm^{-2} (area capacity: 0.1 mAh cm^{-2}, Fig. 3d). The voltage plateau remains flat and stable throughout long-term cycling without significant fluctuation. In contrast, the symmetric Li‖Li batteries with PE exhibit a shorter plating/stripping process around 1200 h (Fig. S14). Furthermore, the surface and cross-sectional deposition structure of the lithium metal was investigated by Scanning Electron Microscopy (SEM). The cycled Li|PE|Li cell presents a loose and non-uniform structure with an uneven surface (Fig. 3e). In contrast, the cycled cell using IGE-2 displays a dendrite-free, compactly aggregated lithium-plating structure with a smooth and flat surface (Fig. 3f). These results indicate that IGE-2 promotes consistent Li^+ deposition, which leads to a dense Li metal layer that effectively mitigates the undesired reaction between Li metal and the electrolyte. These findings were further corroborated by the electrochemical impedance (EIS) measurements. Fig. 3g shows the Nyquist plots with a single complete semicircle. The diameter of the semicircle reflects the interfacial

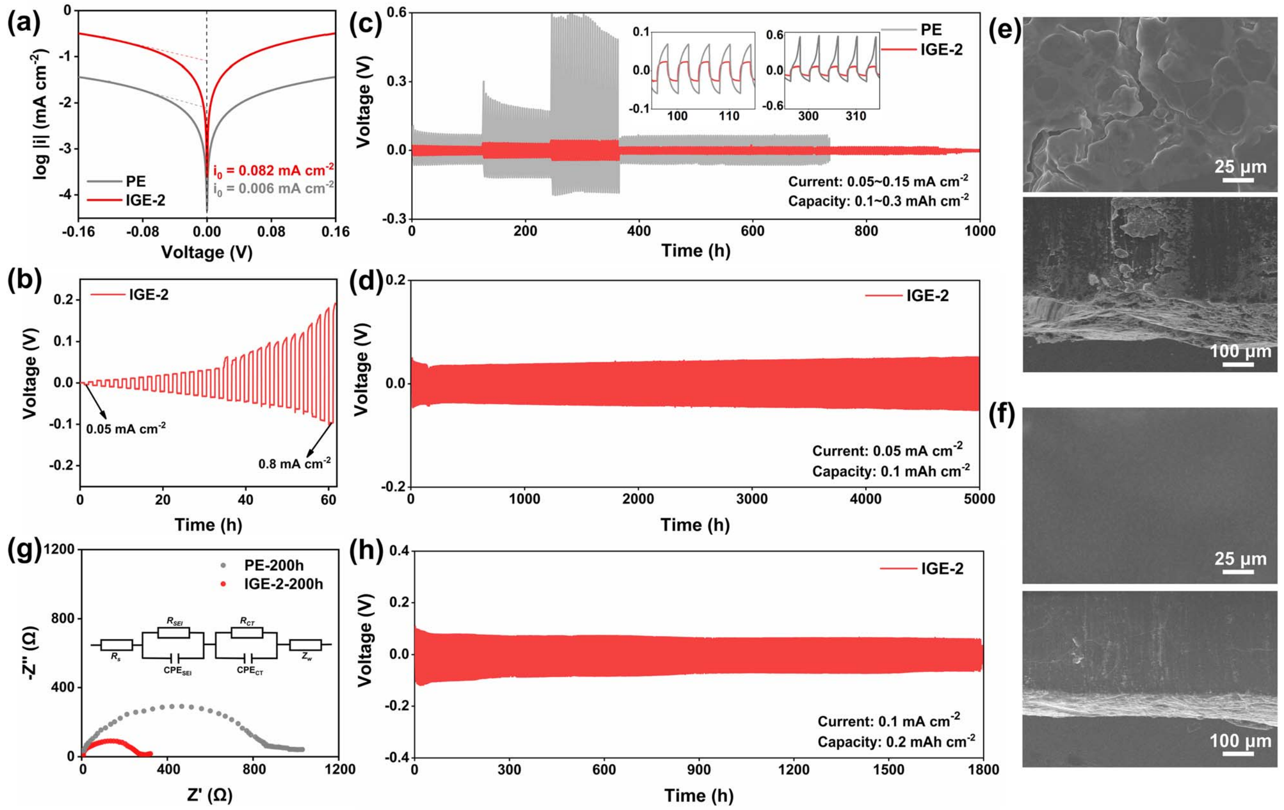

Fig. 3 (a) Tafel plots and (b) CCD tests of Li‖Li cells with PE and IGE-2. (c) Cycling of the Li‖Li cell from 0.05 to 0.15 mA cm^{-2}. (d) Long-term Li plating/stripping process of the Li|IGE-2|Li cell at 0.05 mA cm^{-2}. SEM images from the top view and cross-section of the lithium electrode cycled with (e) PE and (f) IGE-2. (g) Nyquist plots of Li‖Li cells after 200 h of cycling at 0.1 mA cm^{-2}. (h) Long-term Li plating/stripping process of the Li|IGE-2|Li cell at 0.1 mA cm^{-2}.

resistance between the electrolyte and the Li electrode.[49] IGE-2 shows a significantly lower interfacial resistance of 225.7 Ω after 200 h than that of PE (823.4 Ω). The lower interfacial resistance indicates better interfacial compatibility between the Li electrode and IGE-2. Furthermore, the Li|IGE-2|Li cell remains stable for more than 1800 h under 0.1 mA cm^{-2} (0.2 mAh cm^{-2}, Fig. 3h). The remarkable cycling and rate performance of IGE-2 demonstrates superior interfacial compatibility with lithium metal and effective inhibition of the growth of lithium dendrites.

X-ray photoelectron spectroscopy (XPS) etching was carried out to examine the evolution of the SEI components on the Li anode. The C 1s XPS spectrum (Fig. S15) reveals peaks attributed to C–C (284.8 eV), C–O (286.5 eV), C=O (288.6 eV), Li_2CO_3 (289.8 eV), and C–F (291.5 eV). As illustrated in Fig. S15a, the C 1s depth profile for the Li metal cycled with IGE-2 shows that the Li_2CO_3 content increases with etching depth. In contrast, for the Li metal cycled with PE, the Li_2CO_3 content gradually decreases (Fig. S15b), suggesting that the inorganic compounds formed by PE are primarily located in the outer layer. In the F 1s spectrum of Li metal cycled with IGE-2 (Fig. 4a), the signals located at 685.7 eV are attributed to LiF, which increases with depth, suggesting that LiF is primarily located within the inner portion of the SEI. Fig. 4b shows peaks at 688.9 eV (C–F_3) and 690.3 eV (C–F_2), whose intensities increase with etching in the PE-based cell, while the LiF signal decreases. This result is further confirmed in Fig. 4c, which shows an increase in the LiF peak (61.5 eV) in the Li 1s spectrum as the etching depth increases with IGE-2. However, the LiF peak nearly disappears after 120 s of etching for the Li electrode cycled with PE (Fig. 4d).

According to N 1 s (Fig. 4e), $LiNO_3$ (403.1 eV) and Li_3N (400.4 eV) are more evenly distributed across the surface and

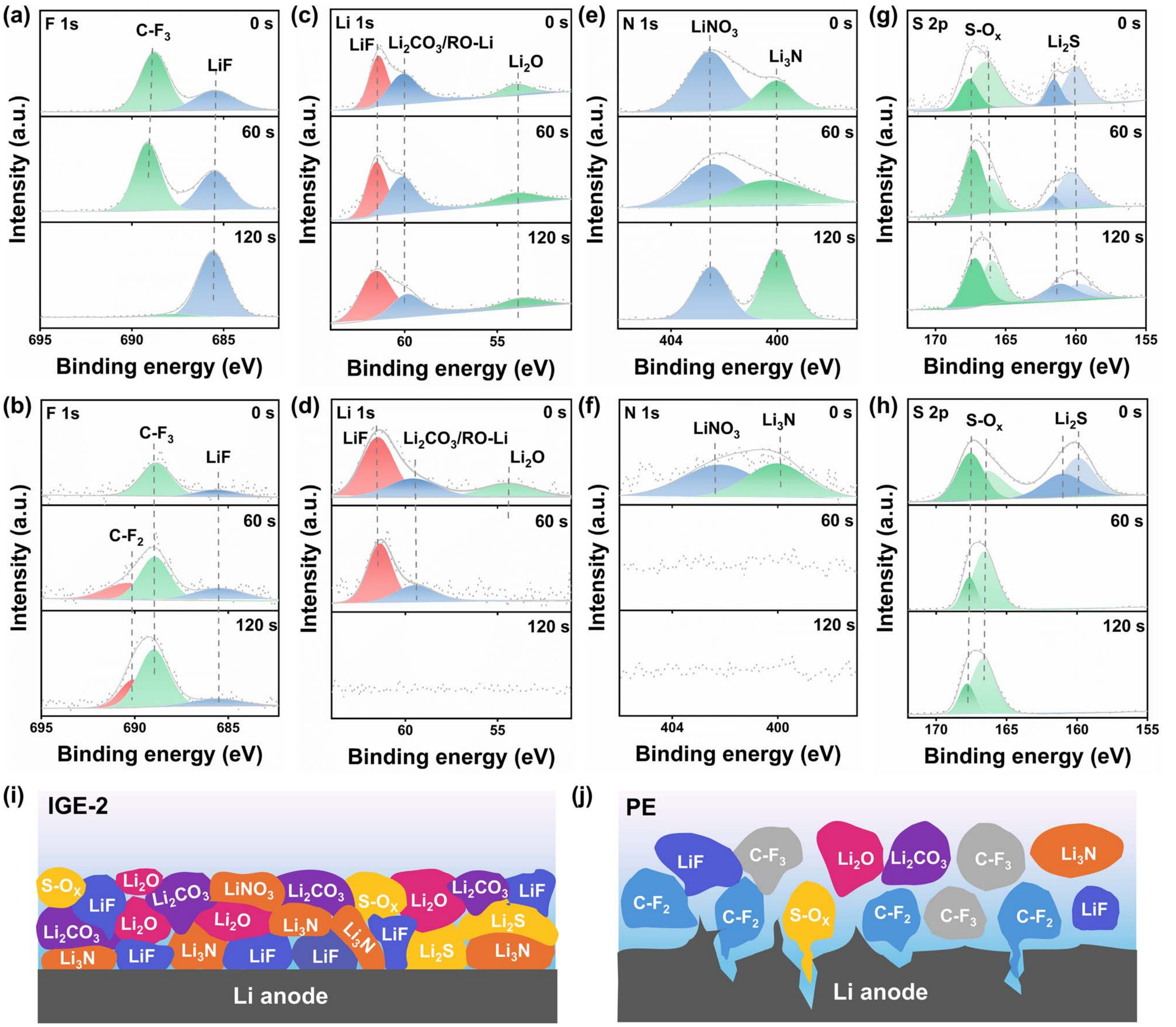

Fig. 4 XPS of cycled Li metal with PE at various etching depths of (a) F 1s, (b) Li 1s, (c) N 1s, and (d) S 2p. XPS of cycled Li metal with IGE-2 at different etching depths of (e) F 1s, (f) Li 1s, (g) N 1s, and (h) S 2p. Schematic illustration of the state of the lithium electrode and the composition of the SEI induced by (i) PE and (j) IGE-2.

depth of the Li metal cycled with IGE-2. These compounds primarily originate from the reductive decomposition of FSI^-/$TFSI^-$, which contributes to a high ionic conductivity SEI layer. In contrast, these compounds are only observed in the outer layer of the SEI for the Li metal cycled with PE (Fig. 4f). Furthermore, the S 2p spectrum identifies diverse inorganic sulfide species, including Li_2S, Li_2SO_3 and Li_2SO_4. Notably, Li_2S is evenly distributed across both the surface and depth of the SEI formed by IGE-2 (Fig. 4g), but it is only found in the external layer of the SEI generated with PE (Fig. 4h). The uniform distribution promotes stable lithium deposition and helps to stabilize the lithium metal anodes. The inorganic layer, enriched with the decomposition products from FSI^-/$TFSI^-$, passivates the anode surface, enabling the maintenance of a robust SEI during prolonged cycles. The higher LiF content within the inner layer contributes to enhanced mechanical strength and interfacial stability.[50] Furthermore, the inorganic-rich inner layer, composed of $LiNO_3$, Li_3N, and Li_2S, promotes efficient Li^+ transfer to the electrode surface due to the high ionic conductivity of these components.[51,52] As illustrated in Fig. 4i, the SEI formed by IGE-2 is denser and more uniform, with a higher level of inorganic components, especially in the inner layer. In comparison, the SEI formed by PE is loose, uneven, and ineffective in suppressing lithium dendrite growth (Fig. 4j). The improvement arises from the strong Li^+–anion interaction within IGE-2, accelerating the decomposition of Li salts and driving the generation of an inorganic-dominated SEI. Consequently, this design enhances mechanical stability, improves ionic conductivity, and ensures a steady and uniform Li^+ deposition.

Electrochemical properties of quasi-solid-state lithium metal batteries

The electrolytes should also demonstrate enhanced oxidative stability and high compatibility with cathodes. Fig. 5a presents the linear sweep voltammogram (LSV) without significant oxidation at 4.6 V, reflecting the superior antioxidation stability of the PE-based electrolytes. Notably, the IGE-2 electrolyte membrane exhibits excellent electrochemical stability, withstanding voltage up to 4.8 V. This high-voltage tolerance is further supported by electrochemical floating tests (Fig. 5b), in which IGE-2 shows significantly lower leakage currents than PE at voltages above 4.5 V, confirming its suitability for high-voltage lithium battery applications.[53] Additionally, IGE-2 achieves a good balance between mechanical properties and electrochemical performance with a tensile stress of 0.8 MPa and a strain of 90%. Meanwhile, it exhibits a high ionic conductivity (9.58×10^{-4} S cm^{-1}), Li^+ transference number (0.78), and electrochemical window (4.8 V) at room temperature, which are higher than those of recently reported quasi-solid polymer electrolytes (QSPEs) or GPEs that are summarized in Table S2. These results underscore the superior electrochemical properties of IGE-2. Furthermore, the ionic conductivity and t_{Li^+} of PE and IGE-2 at 60 °C were tested. As shown in Fig. S16–S19, the ionic conductivity and t_{Li^+} of PE are 1.9×10^{-4} S cm^{-1} and 0.48 at 60 °C, whereas the IGE-2 exhibits a higher ionic conductivity of 1.5×10^{-3} S cm^{-1} and t_{Li^+} of 0.81. As presented in Fig. 5c, the Li|IGE-2|LFP battery consistently delivers stable rate performance, with specific capacities of 156.9, 154.8, 152.1, and 145.3 mAh g^{-1} across current densities of 0.1, 0.3, 0.5, and 1C, respectively. Furthermore, with a reduction in current densities back to 0.1C, the capacity retention is nearly 97% of the initial value, indicating that IGE-2 exhibits high stability at high current rates. In contrast, the Li|PE|LFP cell shows a rapidly fading capacity at 0.5 and 1C, with average capacities of 141.6 and 76.5 mAh g^{-1}, respectively. Fig. 5d highlights the stability over extended cycles of the Li|IGE-2|LFP cells, which deliver a starting capacity value of 152.0 mAh g^{-1} at 0.5C, experiencing a gradual decrease to 120.6 mAh g^{-1} after 1000 cycles, reflecting a capacity retention of 79.3% and a minimal capacity reduction of 0.021% for each cycle. In comparison, the Li|PE|LFP cell exhibits rapid capacity degradation, retaining only 52.7% of its initial capacity after 400 cycles. Additionally, the galvanostatic charging–discharging profiles for the 1st, 3rd, 5th, 10th, and 200th cycles of Li|IGE-2|LFP demonstrate stable charging–discharging plateaus, with a polarization potential of 0.20 V and remaining relatively constant after 200 cycles (Fig. 5e), which indicates reduced polarization and more stable cycling performance compared to the Li|PE|LFP cell (Fig. S20). Furthermore, as shown in Fig. 5f, the IGE-2 electrolyte enables exceptional longevity in both Li||Li and Li||LFP cells, outperforming recently reported QSPEs or GPEs, with the corresponding data detailed in Table S3. It should be attributed to the efficient Li^+ migration pathways, which are facilitated by the abundant cations and anions in the ILs that effectively dissociate the Li salt and coordinate with the free Li^+.[54]

These findings were further corroborated by the EIS tests, which were undertaken to explore the interface evolution during the cycling of the Li||LFP cells (Fig. S21). The Li|IGE-2|LFP battery exhibits a charge-transfer resistance (R_{ct}) of 490.1 Ω after the first cycle, which increases moderately to 755.2 Ω after 20 cycles. In comparison, the R_{ct} of the Li|PE|LFP battery increases from 670.3 to 1076.6 Ω over the same period. The lower interface resistance between IGE-2 and the LFP cathode facilitates ion conduction and ensures efficient Li^+ transport in the Li|IGE-2|LFP battery.[55] Additionally, the complex kinetic processes were further analyzed using the distribution of relaxation times (DRT) (Fig. 5g), derived from the Nyquist-type impedance spectra.[56,57] The DRT plot reveals five peaks within a timescale (τ) range of 10^{-6}–10^{2} s, labeled as R_1–R_5. The τ characterizes each process, while the area under each peak represents the polarization contribution associated with a specific reaction, illustrating variations in the nature and extent of electrode reactions. Generally, the R_4 and R_5 peaks within 10^{-1} to 10 s correspond to the charge-transfer reactions and diffusion impedance, respectively. The R_1, R_2 and R_3 peaks, observed at shorter relaxation times (10^{-5} to 10^{-1} s), are associated with the contact resistance between the cathode and the current collector, as well as ionic conduction through the cathode–electrolyte interphase (CEI) and SEI.[58,59] Notably, the $\gamma(\tau)$ peaks of R_1–R_5 for IGE-2 exhibit shorter τ values than those of PE, indicating that IGE-2 possesses enhanced interfacial

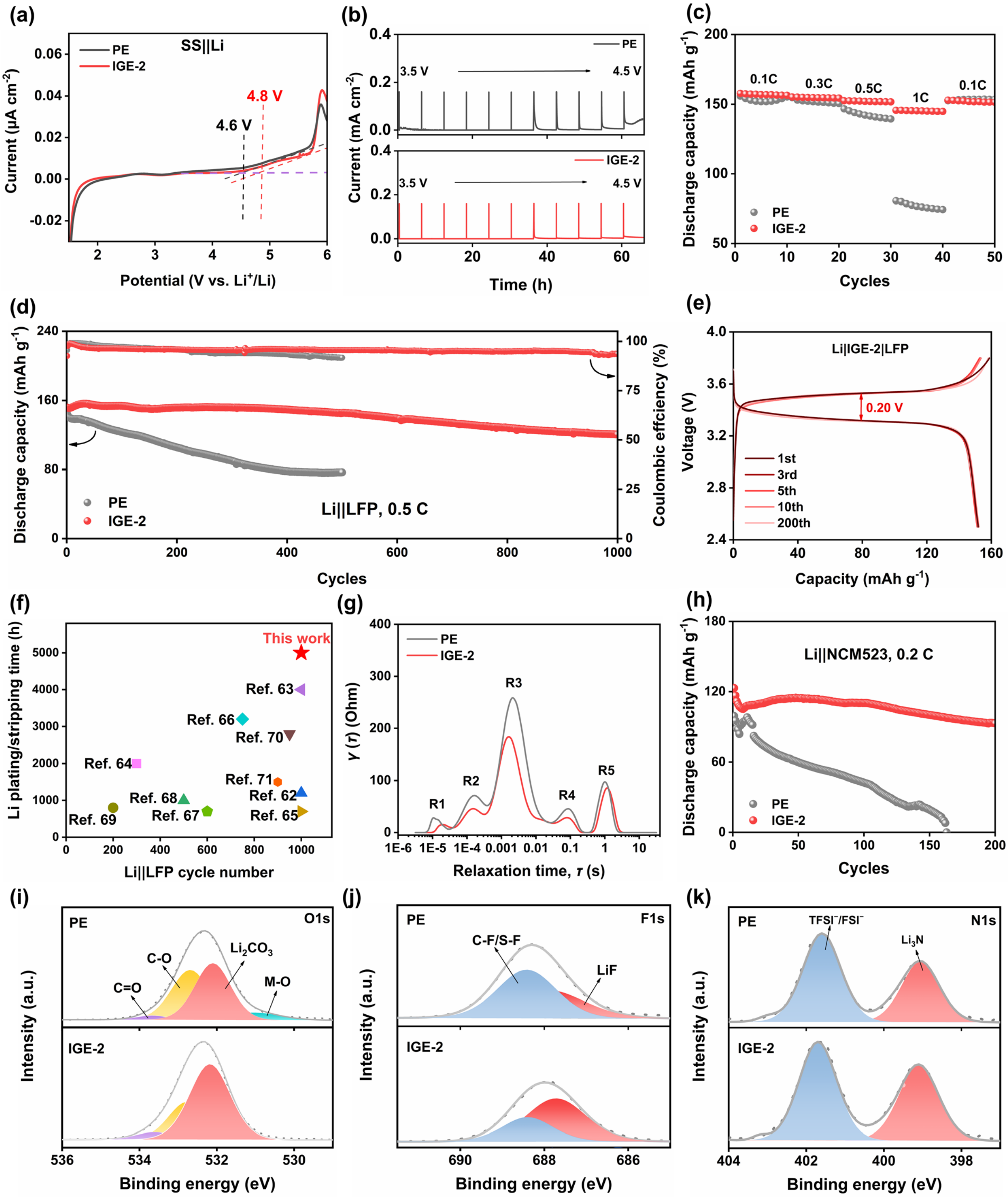

Fig. 5 (a) LSV and (b) floating test of PE and IGE-2. (c) Rate performance of the Li||LFP cell. (d) Discharge specific capacity of the Li||LFP cells at 0.5C. (e) Charge–discharge voltage profile of Li|IGE-2|LFP cells. (f) Comparison of lithium plating/stripping cycling time for Li||Li cells and cycling number of Li||LFP cells with reported QSPEs or GPEs.[62–71] (g) DRT plots of the impedance results. (h) Cycling performance of the Li||NCM523 cells at 0.2C. (i) O 1s, (j) F 1s, and (k) N 1s XPS spectra of NCM523 cathodes after cycling with PE and IGE-2.

reactions, significantly improving interfacial dynamics and providing more efficient pathways for Li$^+$ transport.

Furthermore, the Li|IGE-2|LFP battery with a high mass loading of 9 mg cm^{-2} was tested. As shown in Fig. S22, the cell exhibits an initial specific capacity of 156.8 mAh g^{-1} at a current density of 0.5C and 60 °C. After 100 cycles, it maintains 93.5% of its initial capacity, corresponding to a capacity decay of only 0.065% per cycle, demonstrating that IGE-2 effectively supports high-mass-loading electrodes with excellent cycling stability.

Moreover, to investigate the performance of the high-voltage electrolyte, the Li|IGE-2|NCM523 and Li|PE|NCM523 cells were cycled with a high voltage of 4.2 V at 60 °C. IGE-2 enables stable cycling in the Li||NCM523 batteries, starting with a specific capacity of 123.1 mAh g^{-1} and retaining 75.5% of its capacity over 200 cycles at 0.2C (Fig. 5h), significantly outperforming PE (42.8% capacity retention). These results highlight the significant potential of IGE-2 for reliable applications with high-voltage cathodes. XPS spectroscopy was performed on the cycled NCM523 electrode to investigate the components of the CEI. As shown in Fig. S23, the C 1s spectra of PE and IGE-2 reveal the typical observed components of C–C/C–H (284.8 eV), C–O (285.5 eV), CH_2–CF_2 (287.1 eV), C═O (287.8 eV), and CF_3 (293.0 eV). Compared to the cathode with PE, the cathode with IGE-2 exhibits a higher ratio of the CH_2–CF_2 and CF_3 peaks and a reduced proportion of the C–O and C═O peaks. All these species are attributed to the decomposition of the electrolyte and lithium salt. This trend is further corroborated by the O 1s spectra (Fig. 5i). For IGE-2, the ratios of C–O and C═O decrease, while the proportion of Li_2CO_3 increases from 45.6% to 62.5%. Additionally, the metal–O peak disappears. These changes indicate a greater formation of Li_2CO_3 for the CEI. In the F 1s spectrum (Fig. 5j), the peaks representing LiF (687.9 eV) and C–F/S–F (688.4 eV) are identified. By calculating the integrated peak areas, it is determined that 67.6% of the fluorine in the CEI formed LiF for IGE-2, compared to 42.5% for PE. The C–F/S–F species originate from the FSI^-/$TFSI^-$ anions, while the fluorine source of LiF derives from the decompositions of these anions.[60] The increased proportion of LiF in the cathode interface suggests the formation of a LiF-enriched CEI, which enhances the stability and structural integrity of the interphase and reduces the energy barrier for Li^+ transport through the CEI.[61] As observed in Fig. 5k, the N 1s spectrum displays an increase in the ratio of Li_3N, from 38.2% in the PE-based batteries to 42.6% in the IGE-2-based batteries. These results indicate that IGE-2 promotes the generation of an inorganic CEI enriched with Li_2CO_3, LiF, and Li_3N. Furthermore, the room-temperature performance of the Li|IGE-2|LFP cell is shown in Fig. S24. The Li|IGE-2|LFP cell delivers an initial capacity of 158.9 mAh g^{-1} and stable cycling performance over 100 cycles, maintaining a capacity retention of 85.1%.

Conclusion

In conclusion, an ionogel featuring improved ionic conductivity, an elevated Li^+ transference number, excellent oxidative resistance, and robust mechanical strength was fabricated through a multiple-crosslinking strategy. The multiple-crosslinked network, combined with a regulated Li^+ environment, enabled the construction of rapid Li^+ conductive pathways, while effectively facilitating the formation of an SEI containing a high concentration of LiF and Li_3N. Therefore, it facilitates dendrite-free Li deposition, resulting in Li||Li batteries with outstanding lithium plating/stripping stability for 5000 h. In addition, the Li||LFP cell displays remarkable stability for 1000 cycles at 0.5C. The high-voltage Li||NCM523 cells also exhibit stable cycling with a cut-off voltage of 4.2 V. This study offers a practical application for boosting Li^+ transfer and the interfacial stability of QSPEs for high-performance solid-state LMBs.

Author contributions

J. H., Y. H., F. Y., and X. J. conceived the concept. Y. H. and X. J. supervised the project. J. H. and Y. H. performed the experiments and analyzed the data. Q. G. conducted the MD simulations and DFT calculations. J. H. wrote the manuscript with the help of Y. H., Y. S., J. L., H. H., H. Z., F. Y. and X. J. All the authors discussed the results and commented on the manuscript.

Conflicts of interest

There are no conflicts to declare.

Data availability

The data supporting this article have been included as part of the supplementary information (SI). Supplementary information: additional analysis details, Fig. S1–S24 and Tables S1–S3 as described in the main text. See DOI: **https://doi.org/10.1039/d5ta07159c**.

Acknowledgements

This work was supported by the Swedish Energy Agency (P2022-00014). J. Huang and X. Ji acknowledge the financial support from STINT (CH2019-8287) and Bio4Energy, Y. Hu and X. Ji acknowledge the financial support from the Kempe Foundation (JCSMK23-0333), and Y. Hu would like to thank the National Natural Science Foundation of China (52333002, 52503102) and Natural Science Foundation of Jiangsu Province (BK20240805) for their support.

Notes and references

1 T. Deng, L. Cao, X. He, A. M. Li, D. Li, J. Xu, S. Liu, P. Bai, T. Jin, L. Ma, M. A. Schroeder, X. Fan and C. Wang, *Chem*, 2021, **7**, 3052–3068.
2 S. Li, Q. Liu, W. Zhang, L. Fan, X. Wang, X. Wang, Z. Shen, X. Zang, Y. Zhao, F. Ma and Y. Lu, *Adv. Sci.*, 2021, **8**, 2003240.
3 H. Duan, Y. X. Yin, Y. Shi, P. F. Wang, X. D. Zhang, C. P. Yang, J. L. Shi, R. Wen, Y. G. Guo and L. J. Wan, *J. Am. Chem. Soc.*, 2018, **140**, 82–85.
4 S. Zhang, F. Sun, X. Du, X. Zhang, L. Huang, J. Ma, S. Dong, A. Hilger, I. Manke, L. Li, B. Xie, J. Li, Z. Hu, A. C. Komarek, H. J. Lin, C. Y. Kuo, C. T. Chen, P. Han, G. Xu, Z. Cui and G. Cui, *Energy Environ. Sci.*, 2023, **16**, 2591–2602.
5 Y. Ma, J. Wan, Y. Yang, Y. Ye, X. Xiao, D. T. Boyle, W. Burke, Z. Huang, H. Chen, Y. Cui, Z. Yu, S. T. Oyakhire and Y. Scalable Cui, *Adv. Energy Mater.*, 2022, **12**, 2103720.
6 H. Wang, Z. Yu, X. Kong, S. C. Kim, D. T. Boyle, J. Qin, Z. Bao and Y. Cui, *Joule*, 2022, **6**, 588–616.

7 W. Zhang, V. Koverga, S. Liu, J. Zhou, J. Wang, P. Bai, S. Tan, N. K. Dandu, Z. Wang, F. Chen, J. Xia, H. Wan, X. Zhang, H. Yang, B. L. Lucht, A. M. Li, X. Q. Yang, E. Hu, S. R. Raghavan, A. T. Ngo and C. Wang, *Nat. Energy*, 2024, **9**, 386–400.

8 D. Wu, C. Zhu, H. Wang, J. Huang, G. Jiang, Y. Yang, G. Yang, D. Tang and J. Ma, *Angew. Chem., Int. Ed.*, 2024, **63**, e202315608.

9 Z. Y. Wang, C. Z. Zhao, N. Yao, Y. Lu, Z. Q. Xue, X. Y. Huang, P. Xu, W. Z. Huang, Z. X. Wang, J. Q. Huang and Q. Zhang, *Angew. Chem., Int. Ed.*, 2025, **64**, e202414524.

10 X. Lu, Y. Wang, X. Xu, B. Yan, T. Wu and L. Lu, *Adv. Energy Mater.*, 2023, **13**, 2301746.

11 X. Xie, Z. Wang, S. He, K. Chen, Q. Huang, P. Zhang, S.-M. Hao, J. Wang and W. Zhou, *Angew. Chem., Int. Ed.*, 2023, **135**, e202218229.

12 M. Yao, Q. Ruan, S. Pan, H. Zhang and S. Zhang, *Adv. Energy Mater.*, 2023, **13**, 2203640.

13 Y. Liu, Z. Jin, Z. Liu, H. Xu, F. Sun, X. Q. Zhang, T. Chen and C. Wang, *Angew. Chem., Int. Ed.*, 2024, **63**, e202405802.

14 H. Liang, L. Wang, A. Wang, Y. Song, Y. Wu, Y. Yang and X. He, *Nano-Micro Lett.*, 2023, **15**, 42.

15 Z. Y. Wang, C. Z. Zhao, S. Sun, Y. K. Liu, Z. X. Wang, S. Li, R. Zhang, H. Yuan and J. Q. Huang, *Matter*, 2023, **6**, 1096–1124.

16 K. Mu, D. Wang, W. Dong, Q. Liu, Z. Song, W. Xu, P. Yao, Y. Chen, B. Yang, C. Li, L. Tian, C. Zhu and J. Xu, *Adv. Mater.*, 2023, **35**, 2304686.

17 X. Shan, Z. Song, H. Ding, L. Li, Y. Tian, A. P. Sokolov, M. Tian, K. Xu and P. F. Cao, *Energy Environ. Sci.*, 2024, **17**, 8457–8481.

18 S. Wang, Y. Jiang and X. Hu, *Adv. Mater.*, 2022, **34**, 2200945.

19 F. Q. Liu, W. P. Wang, Y. X. Yin, S. F. Zhang, J. L. Shi, L. Wang, X. D. Zhang, Y. Zheng, J. J. Zhou, L. Li and Y. G. Guo, *Sci. Adv.*, 2018, **4**, eaat5383.

20 F. Liu, J. Wang, W. Chen, M. Yuan, Q. Wang, R. Ke, G. Zhang, J. Chang, C. Wang, Y. Deng, J. Wang and M. Shao, *Adv. Mater.*, 2024, **36**, 2409838.

21 C. Zhang, Z. Lu, M. Song, Y. Zhang, C. Jing, L. Chen, X. Ji and W. Wei, *Adv. Energy Mater.*, 2023, **13**, 2203870.

22 L. Yu, L. Yu, Q. Liu, T. Meng, S. Wang and X. Hu, *Adv. Funct. Mater.*, 2022, **32**, 2110653.

23 X. Ma, J. Yu, Y. Hu, J. Texter and F. Yan, *Ind. Chem. Mater.*, 2023, **1**, 39–59.

24 A. J. D'Angelo and M. J. Panzer, *Adv. Energy Mater.*, 2018, **8**, 1801646.

25 D. Xu, D. Zhao, X. Niu, T. Wang and Z. Yang, *Chem. Eng. J.*, 2024, **490**, 151780.

26 T. Zhou, Y. Zhao and J. W. Choi, *Angew. Chem., Int. Ed.*, 2021, **60**, 22791–22796.

27 Y. Qin, H. Wang, J. Zhou, R. Li, C. Jiang, Y. Wan, X. Wang, Z. Chen, X. Wang, Y. Liu, B. Guo and D. Wang, *Angew. Chem., Int. Ed.*, 2024, **63**, e202402456.

28 Z. Liu, H. Wang, H. Cao, D. Xie, C. Li, H. Yang, W. Yao and A. K. Cheetham, *Adv. Mater.*, 2022, **34**, 2203332.

29 X. Pei, Y. Li, T. Ou, X. Liang, Y. Yang, E. Jia, Y. Tan and S. Guo, *Angew. Chem., Int. Ed.*, 2022, **61**, e202205075.

30 X. Wang, F. Chen, G. M. A. Girard, H. Zhu, D. R. MacFarlane, D. Mecerreyes, M. Armand, P. C. Howlett and M. Forsyth, *Joule*, 2019, **3**, 2687–2702.

31 Q. Zhang, T. Bian, X. Wang, R. Shi and Y. Zhao, *Angew. Chem., Int. Ed.*, 2025, **64**, e202415343.

32 Y. Wei, T.-H. Liu, W. Zhou, H. Cheng, X. Liu, J. Kong, Y. Shen, H. Xu and Y. Huang, *Adv. Energy Mater.*, 2023, **13**, 2203547.

33 A. Wang, S. Geng, Z. Zhao, Z. Hu and J. Luo, *Adv. Funct. Mater.*, 2022, **32**, 2201861.

34 C. Yan, P. Zhu, H. Jia, Z. Du, J. Zhu, R. Orenstein, H. Cheng, N. Wu, M. Dirican and X. Zhang, *Energy Storage Mater.*, 2020, **26**, 448–456.

35 Y. Hu, L. Li, H. Tu, X. Yi, J. Wang, J. Xu, W. Gong, H. Lin, X. Wu and M. Liu, *Adv. Funct. Mater.*, 2022, **32**, 2203336.

36 H. Chen, K. Chen, L. Luo, X. Liu, Z. Wang, A. Zhao, H. Li, X. Ai, Y. Fang and Y. Cao, *Angew. Chem., Int. Ed.*, 2024, **63**, e202316966.

37 C. D. Fang, Y. Huang, Y. F. Sun, P. F. Sun, K. Li, S.-Y. Yao, M.-Y. Zhang, W. H. Fang and J. J. Chen, *Nat. Commun.*, 2024, **15**, 6781.

38 Q. Wang, J. Yang, X. Huang, Z. Zhai, J. Tang, J. You, C. Shi, W. Li, P. Dai, W. Zheng, L. Huang and S. Sun, *Adv. Energy Mater.*, 2022, **12**, 2103972.

39 Y. Wang, Y. Ni, S. Xu, Y. Lu, L. Shang, Z. Yang, K. Zhang, Z. Yan, W. Xie and J. Chen, *J. Am. Chem. Soc.*, 2025, **147**, 10772–10783.

40 Y. Wang, T. Li, X. Yang, Q. Yin, S. Wang, H. Zhang and X. Li, *Adv. Energy Mater.*, 2024, **14**, 2303189.

41 X. Ma, J. Yu, X. Zou, X. Wang, H. Wang, Y. Hu, M. Duan, S. Tao, S. Sun, Y. Shen and F. Yan, *Angew. Chem., Int. Ed.*, 2025, **64**, e202505035.

42 J. Li, Z. Hu, S. Zhang, H. Zhang, S. Guo, G. Zhong, Y. Qiao, Z. Peng, Y. Li, S. Chen, G. Chen and A. M. Cao, *Nat. Sustain.*, 2024, **7**, 1481–1491.

43 W. Yang, Y. Liu, X. Sun, Z. He, P. He and H. Zhou, *Angew. Chem., Int. Ed.*, 2024, **63**, e202401428.

44 F. Chen, X. Wang, M. Armand and M. Forsyth, *Nat. Mater.*, 2022, **21**, 1175–1182.

45 F. Chen, P. Howlett and M. Forsyth, *J. Phys. Chem. C*, 2018, **122**, 105–114.

46 K. Liu, H. Cheng, Z. Wang, Y. Zhao, Y. Lv, L. Shi, X. Cai, Z. Cheng, H. Zhang and S. Yuan, *Adv. Energy Mater.*, 2024, **14**, 2303940.

47 R. Xu, F. Liu, Y. Ye, H. Chen, R. R. Yang, Y. Ma, W. Huang, J. Wan and Y. Cui, *Adv. Mater.*, 2021, **33**, 2104009.

48 H. Wang, Y. Yang, C. Gao, T. Chen, J. Song, Y. Zuo, Q. Fang, T. Yang, W. Xiao, K. Zhang, X. Wang and D. Xia, *Nat. Commun.*, 2024, **15**, 2500.

49 C. Fu, G. Homann, R. Grissa, D. Rentsch, W. Zhao, T. Gouveia, A. Falgayrat, R. Lin, S. Fantini and C. Battaglia, *Adv. Energy Mater.*, 2022, **12**, 2200412.

50 Z. Sun, Y. Wang, S. Shen, X. Li, X. Hu, M. Hu, Y. Su, S. Ding and C. Xiao, *Angew. Chem., Int. Ed.*, 2023, **62**, e202309622.

51 J. Wang, L. Xie, W. Wu, Y. Liang, M. Cao, C. Gao, Y. Bo, J. Zhang and J. Zhang, *Energy Environ. Sci.*, 2024, **17**, 9100–9111.

52 S. Xu, S. Xu, X. Guo, J. Xiong, Z. Wei, S. Zhu, J. Xu, S. Gong, P. Shi, S. Guo and Y. Min, *Adv. Funct. Mater.*, 2025, **35**, 2500335.

53 Y. Wang, S. Chen, Z. Li, C. Peng, Y. Li and W. Feng, *Energy Storage Mater.*, 2022, **45**, 474–483.

54 M. Egashira, H. Todo, N. Yoshimoto and M. Morita, *J. Power Sources*, 2008, **178**, 729–735.

55 H. X. Yang, Z. K. Liu, Y. Wang, N. W. Li and L. Yu, *Adv. Funct. Mater.*, 2023, **33**, 2209837.

56 Y. Lu, C. Z. Zhao, J. Q. Huang and Q. Zhang, *Joule*, 2022, **6**, 1172–1198.

57 H. Da, S. Pan, J. Li, J. Huang, X. Yuan, H. Dong, J. Liu and H. Zhang, *Energy Storage Mater.*, 2023, **56**, 457–467.

58 X. Cai, C. Zhang, H. Ruan, Z. Chen, L. Zhang, D. U. Sauer and W. Li, *Adv. Sci.*, 2024, **11**, 2406934.

59 R. Soni, J. B. Robinson, P. R. Shearing, D. J. L. Brett, A. J. E. Rettie and T. S. Miller, *Energy Storage Mater.*, 2022, **51**, 97–107.

60 X. Zhou, F. Huang, X. Zhang, B. Zhang, Y. Cui, Z. Wang, Q. Yang, Z. Ma and J. Liu, *Angew. Chem., Int. Ed.*, 2024, **63**, e202401576.

61 L. Hong, Y. Zhang, P. Mei, B. Ai, Y. Zhang, C. Zhou, X. Bao and W. Zhang, *Angew. Chem., Int. Ed.*, 2024, **63**, e202409069.

62 X. Deng, J. Chen, X. Jia, X. Da, Y. Zhao, Y. Gao, Y. Gao, X. Kong, S. Ding and G. Gao, *Angew. Chem., Int. Ed.*, 2024, **63**, e202410818.

63 J. Li, C. Li, Y. Yao, Z. Li, J. Yao, L. Luo, W. Liao, X. Ye, W. Dai, F. Li, X. Zhang and Y. Xiang, *Adv. Energy Mater.*, 2024, **14**, 2402362.

64 W. Huang, S. Wang, X. Zhang, Y. Kang, H. Zhang, N. Deng, Y. Liang and H. Pang, *Adv. Mater.*, 2023, **35**, 2310147.

65 W. Min, L. Li, M. Wang, S. Ma, H. Feng, W. Wang, H. Ding, T. Cheng, Z. Li, T. Saito, H. Yang and P. F. Cao, *Angew. Chem., Int. Ed.*, 2025, **64**, e202422510.

66 S. Zhang, Z. Li, Y. Zhang, X. Wang, P. Dong, S. Lei, W. Zeng, J. Wang, X. Liao, X. Chen, D. Li and S. Mu, *Energy Environ. Sci.*, 2025, **18**, 3807–3816.

67 S. Guo, Y. Su, K. Yan, C. Zhao, Y. Lu, H. Wang, J. Dong, N. Li, Y. Liu, Y. Guan, F. Wu and L. Chen, *Adv. Sci.*, 2024, **11**, 2404307.

68 W. Ma, Y. Guo, J. Sun, C. Zhang, Y. Zhu, H. Sun, L. Huang, Z. Hu, H. Wang, M. Zhu and G. Wang, *Angew. Chem., Int. Ed.*, 2025, **64**, e202418999.

69 D. Chen, M. Zhu, P. Kang, T. Zhu, H. Yuan, J. Lan, X. Yang and G. Sui, *Adv. Sci.*, 2022, **9**, 2103663.

70 L. Zhu, J. Chen, Y. Wang, W. Feng, Y. Zhu, S. F. H. Lambregts, Y. Wu, C. Yang, E. R. H. Van Eck, L. Peng, A. P. M. Kentgens, W. Tang and Y. Xia, *J. Am. Chem. Soc.*, 2024, **146**, 6591–6603.

71 Z. Ren, J. Li, M. Cai, R. Yin, J. Liang, Q. Zhang, C. He, X. Jiang and X. Ren, *J. Mater. Chem. A*, 2023, **11**, 1966–1977.